C. R. Physique 16 (2015) 819–835

Contents lists available at ScienceDirect

Comptes Rendus Physique

www.sciencedirect.com

Radio science for connecting humans to information systems / L'homme connecté

Coils for ingestible capsules: Near-field magnetic induction link

Boucles pour gélules ingérables : bilan de liaison en champ proche

Marjorie Grzeskowiak [a,*], Fatiha El Hatmi [a], Antoine Diet [b], Megdouda Benamara [a], David Delcroix [a], Thierry Alves [a], Stéphane Protat [a], Shermila Mostarshedi [a], Odile Picon [a], Yann Le Bihan [b,1], Gaelle Lissorgues [a]

[a] *ESYCOM (EA 2552), UPEM, ESIEE-Paris, CNAM, 77454 Marne-la-Vallée cedex, France*
[b] *GEEPS (UMR 8507), Université Paris Saclay, CNRS, Centrale-Supélec, Université Paris-Sud, UPMC, rue Juliot-Curie, plateau de Moulon, 91192 Gif-sur-Yvette, France*

ARTICLE INFO

Article history:
Available online 29 September 2015

Keywords:
Mutual inductance
Magnetic induction link budget
Monolayer and multilayer stacked coil
On-body spiral coil
Wireless ingestible capsule

Mots-clés :
Inductance mutuelle
Bilan de liaison par induction magnétique
Boucle monocouche et multicouche
Boucle spirale sur le corps
Gélule ingérable sans fil

ABSTRACT

Monolayer- and compact-multilayer-stacked ingestible TX coils are investigated for ingestible capsule systems. The inductive link through the human body is modeled. The efficiency of the near-field magnetic induction link budget is evaluated in the air, in the homogeneous human body and in the three-layer human body. The variations of the position and the orientation of the TX capsule coil are taken into account to evaluate the coupling response between the TX ingestible and RX on-body coils.

RÉSUMÉ

Des boucles monocouches et multicouches compactes sont étudiées pour des systèmes de gélules ingérables. Le lien inductif à travers le corps humain est modélisé. L'efficacité du bilan de liaison en champ proche par induction magnétique est évalué dans l'air, dans le corps humain homogène et dans le corps humain trois couches. Les variations de la position et de l'orientation de la boucle dans la gélule d'émission sont prises en compte pour évaluer la réponse de couplage entre les boucles d'émission dans la gélule ingérable et de réception sur le corps humain.

1. Introduction

Wireless ingestible capsule devices get more and more used as a tool for cancer diagnosis and medical treatments of diseases of the gastro intestinal (GI) tract [1]. These systems were proposed to overcome the limited test coverage, because

* Corresponding author.
E-mail addresses: Marjorie.Grzeskowiak-lucas@u-pem.fr, marjorie.grzeskowiak@univ-mlv.fr, grzeskow@univ-mlv.fr (M. Grzeskowiak).
[1] Member IEEE.

http://dx.doi.org/10.1016/j.crhy.2015.07.009
1631-0705/

Table 1
Specifications of antennas for ingestible systems.

Working frequency	Size $\phi^x h$ (in λ_0)	Path loss (capsule inside human body, 5 cm away from the external surface)	Bandwidth (in %)	Reference
460 MHz–535 MHz	4 mm × 10 mm (0.0066 λ_0 × 0.0166 λ_0)	Ø	75 MHz (15%)	[2]
32 MHz 40 MHz	1 mm × 1 mm × 0.5 mm (0.00013 λ_0 × 0.000013 λ_0 × 0.00006 λ_0)	Attenuation from 1 dB to 5 dB and no channel fading	Ø	LF1 [4] LF2 [4]
868 MHz 869 MHz	7 mm × 0.5 mm (0.020 λ_0 × 0.0028λ_0) 27 mm × 13 mm × 1.5 mm (0.078 λ_0 × 0.037 λ_0 × 0.0043 λ_0)	Attenuation from 15 dB to 26 dB and channel fading up to 52 dB	Ø	HF1 [4] HF2 [4]
1.4 GHz	Antenna conformed on 10 mm × 26 mm (0.046 λ_0 × 0.1214 λ_0)	Peak gain = −28.4 dBi; $\eta = 0.05\%$	Ø	[6] and [8]
404.5 MHz 2.387 GHz	10 mm × 32.1 mm (0.013 λ_0 × 0.043 λ_0) 10 mm × 32.1 mm (0.08 λ_0 × 0.2568 λ_0)	Peak gain = −28.8 dBi; $\eta = 0.058\%$ Peak gain = −18.5 dBi; $\eta = 0.9\%$	401–406 MHz (2.3%) 2.4–2.5 GHz (6%)	[14]
2.4 GHz	11 mm × 3.81 mm (0.088 λ_0 × 0.030 λ_0)	Peak gain = −26.7 dBi	26%	[17]

of finite length of wired systems, and thus reduce the discomfort and pain of the patients [2–4]. A wireless capsule usually includes sensors, IC chip with an antenna, battery and is used to transmit physiological information from the GI tract, such as temperature [9], pressure, pH, and oxygen concentration [5,6], to provide drug to the patient [7,8], and to send real-time GI tract images at high data rate for video endoscopic capsule [5–9]. Capsule systems require having a small size to be swallowed by patients. The design of electrically small coils that limit efficiency is a challenging task: efficiency can affect power consumption, which must be reduced since the small-size battery contains limited energy. The wireless link is considered in the presence of a "hostile" environment such as the human body. Inductive links for providing energy to ingestible capsule [11–14] are investigated in the laboratory. In the present study, the system seems to be suited to ambulatory, i.e., out-of-the-laboratory devices: batteries inserted in capsule could transfer energy (and potential data of sensor) to a received belt or cover and the system could permit capturing physiological data in real time and as conveniently as possible, with a relative cheap ambulatory system of sensors and wearables.

The near-field system employs MI (magnetic induction) between the TX and RX coils. Because of the mutual inductance, the coils act as a magnetically coupled transformer. The magnetic field penetrates high-permittivity materials, such as the human body, better than electromagnetic waves that suffer from high power absorption [15] and lead to low antenna radiation efficiency [10–21]. Table 1 synthesizes the specification of existing capsule antennas in term of resonant frequency, size, path loss and frequency bandwidth and confirms in measurement [4] that magnetically coupled near-field communication systems present an attractive option for future applications with the advantages of ingestible capsules miniaturization (at one eighth of the volume of the 868-MHz scheme), no channel fading, and allows four times the battery life of the 868-MHz ingestible systems.

In this paper, a near-field MI is characterized between the TX capsule coil and the RX spiral coil outside the human body. In the first part, the near-field MI link budget is expressed from the coils' parameters and an equivalent electrical circuit is modeled using ADS software [22]. Then, the mutual inductance between TX and RX coils is calculated versus the size of the RX coils size, the lateral misalignment and the angular misalignment of the TX coil. In a following section, a TX capsule one-layer coil is designed at 40.68 MHz. The efficiency of the link is evaluated from simulated results in the homogeneous human body versus the orientation and position of the capsule coil and in a three-layered model of human body. In the last part, to improve the performances of the inductive link, the size of the RX spiral coil is increased and the TX capsule becomes a five-layer structure. The efficiency of the link is simulated and measured in the air and in the tissue-simulating liquid versus the frequency, versus the distance between coaxial coils and versus the lateral and angular misalignment.

2. Near-field MI link

The TX and RX coils are supposed to be placed respectively In and On Body. The impact of the media (human body or air) is seen in the modification of the RF wave's attenuation, which is the real part of the complex propagation constant (1). The relative permittivity and the conductivity of the tissue-simulating muscle are calculated thanks to the 4-Cole–Cole model

[23,29], and are respectively equal to 83 and 0.67 S/m. In the air, these parameters are considered to be equal to 1 for the relative permittivity and to 0 for the conductivity.

$$\gamma = \alpha + \mathrm{j}\beta = \mathrm{j}\omega\sqrt{\mu\varepsilon_0\varepsilon_\mathrm{r}}\sqrt{1 - \mathrm{j}\frac{\sigma}{\omega\varepsilon_0\varepsilon_\mathrm{r}}} \tag{1}$$

The average attenuation is equal to 0.78 dB/cm in the human body. The signal transmission at 5 cm from the air to the human body could be decreased by 3.92 dB. In a non-conductive medium, such as air, or the human body with null conductivity, the attenuation is similar and equal to zero: at 40.68 MHz, the medium attenuation depends essentially on its conductivity. By taking into account the distance of 5 cm between the TX and RX coils, the RX coil is placed in non-radiative near-field of the TX coil and so the MI near field phenomenon is studied in the following part. The magnetic field strength on the (z) axis, generated by a current-carrying coil in XY plane is quantified by the mathematical expression (2) and depends on the intensity of the current (I), the loop radius (R), the number of the loop turns (N) and the distance (z) from the center of the coil in the normal direction [24,25]:

$$H(z) = \frac{I \times N \times R^2}{2 \times (R^2 + z^2)^{3/2}} \tag{2}$$

The classic very-near-field zone D is limited to $D << \lambda/2\pi$ for the operating central frequency f. At 40.68 MHz, the wavelength is reduced from 750 cm in the air to 53 cm in the human body, while considering $\varepsilon_\mathrm{r} = 83$ for the dielectric characteristics of the muscle. Since the average distance between the small intestine and the on-body surface is superior to 5 cm, the limit D of 8.5 cm ($= \lambda/2\pi = 53$ cm$/2\pi$) is acceptable for ingestible systems in this case. The dimensions of the TX coil, operating inside the GI tract, are limited by the size of the capsule in which it will be encased. The diameter of the capsule is about 10.5 mm and its length is about 25 mm [2]. So, the in-body antenna diameter must be smaller than 10.1 mm. The coils in near-field are characterized by the following parameters: the coupling coefficient (k) between the transmitter and the receiver, the inductance L of the coils, and the loaded quality Q factor of the coils. In a first step, the coils are designed with the optimized parameters: the geometry and dimensions of the coils, the section of the wire and the number of turns by empirical formulas. The coil resistance R increases with the number of turns. A low-quality Q factor will result in a weaker energy transfer. In contrast, Q, which is inversely proportional to the bandwidth, allows, in this case, high data transfer. In order to estimate empirically the voltage level V_R (3) received by the RX coil, a near-field MI link budget has been carried out using:

$$V_R^2(\omega) = V_\mathrm{T}^2\eta_\mathrm{T}\eta_\mathrm{R}Q_\mathrm{T}Q_\mathrm{R}k^2(d) \tag{3}$$

$$k^2(d) = \frac{r_\mathrm{T}^3 \times r_\mathrm{R}^3 \times \pi^2}{(r_\mathrm{T}^2 + d^2)^3} \tag{4}$$

where η_T and η_R are the resistive efficiencies Q_T, and Q_R are the loaded quality factors, Q_uT, and Q_uR are the unloaded quality factors and r_T and r_R are the radii of the transmitter and of the receiver coils. The formula (4) of k is empirical and is used when the coils are coaxially positioned in free-space, where η_T, η_R, Q_T, Q_R, Q_uT, Q_uR and k can be given as:

$$\eta_\mathrm{T} = \frac{R_\mathrm{S}}{R_\mathrm{S} + R_\mathrm{LT}}; \qquad \eta_\mathrm{R} = \frac{R_\mathrm{L}}{R_\mathrm{L} + R_\mathrm{LR}} \tag{5}$$

$$Q_\mathrm{T} = \frac{\omega_0 L_\mathrm{T}}{R_\mathrm{S} + R_\mathrm{LT}}; \qquad Q_\mathrm{R} = \frac{\omega_0 L_\mathrm{R}}{R_\mathrm{L} + R_\mathrm{LR}}; \qquad Q_\mathrm{uT} = \frac{\omega_0 L_\mathrm{T}}{R_\mathrm{LT}}; \qquad Q_\mathrm{uR} = \frac{\omega_0 L_\mathrm{R}}{R_\mathrm{LR}} \tag{6}$$

$$k = \frac{M}{\sqrt{L_\mathrm{T}L_\mathrm{R}}} \tag{7}$$

The coupling coefficient k in (7) depends on the medium conductivity and on the mutual inductance, whose value varies as a function of the position and orientation of both coils. The coupling coefficient, calculated in (7) by a simulation with an electromagnetic software and measured with a VNA (Vector Network Analyzer) is more accurate than the one determined by the empirical formula (4). R_LT and R_LR are the resistances of the transmitter and the receiver coils, respectively, R_S and R_L are the source and the load resistances, L_T and L_R the inductances of the transmitter and of the receiver coils and M is the mutual inductance. The near-field system can be modeled with the Keysight-ADS software. The equivalent circuit model, including the TX capsule and RX on-body coils is presented in Fig. 1 [22]. L-match circuits, using lumped capacitances C, form the matching networks, in order to match the impedance between the source and the capsule coil, and between the on-body coil and the load. The source and load impedances correspond to 50 Ω in a standard measurement.

In the following section, we focus on the mutual inductance to study theoretically the coupling efficiency versus the relative size, lateral and angular misalignment between the coils in the air.

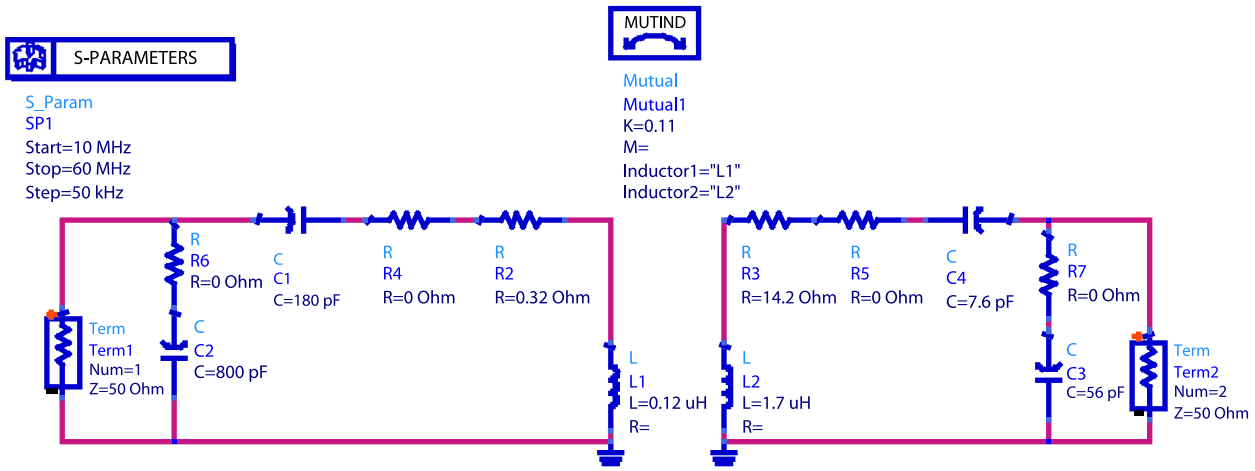

Fig. 1. (Color online.) Inductively coupled equivalent circuit model in ADS software.

3. Mutual inductance considerations

To theoretically study the magnetic coupling in the air, the mutual inductance between the coils is calculated. For simplicity, we focus on the case of a one-turn coil, represented by a circular loop 1 cm in diameter for the TAG, and by a square loop of length L for the reader. The square loop can define a surface on which the magnetic flux is integrated easily [26,27]. As the mutual inductance is reciprocal, the circular loop is considered generating the B-field by a current circulation i_1 on the loop. The magnetic field (B_r, B_θ, B_y) evaluated in the (x, y, z) position [27], generated by a circular loop of radius R positioned in the $(Y0Z)$ plane (Fig. 2), centered in $(0, 0, 0)$ is expressed by equation (8):

$$\left\{\begin{array}{l} B_r = \dfrac{i_1\mu_0 y}{2\pi[(R+r)^2+y^2]^{1/2}r}\left[\dfrac{R^2+r^2+y^2}{[(R-r)^2+y^2]}E(p)-K(p)\right] \\ B_\theta = 0 \\ B_y = \dfrac{i_1\mu_0}{2\pi[(R+r)^2+y^2]^{1/2}r}\left[\dfrac{R^2-r^2-y^2}{[(R-r)^2+y^2]}E(p)+K(p)\right] \\ p^2 = \dfrac{4Rr}{[(R+r)^2+y^2]} \end{array}\right\} \tag{8}$$

where r corresponds to the distance between the center of the circular loops and the functions $K(p)$ and $E(p)$ are the complete elliptic integral of first and second kinds, respectively. By discretizing (1), with a 500-μm pace, the mutual inductance can be calculated with MATLAB.

3.1. TAG parallel configuration

When the coils are perfectly aligned and spaced with a distance d, as seen in Fig. 2, the mutual inductance between the coils is reported versus the length of the square loop, for different distances d. The mutual inductance (noted M) depends on the length of the square loop for a given distance. When the distance increases, the length of the square loop has to be increased to optimize the mutual inductance. However, by considering the optimum value of M for each value of d, the maximum value decreases when the length L increases. For a wireless ingestible capsule in the small intestine, we consider a distance of 5 cm between the coils. In this case, increasing the square loop side from 4 to 7 cm allows multiplying the mutual inductance by 2.15.

3.2. TAG normal configuration

Furthermore, when the planes of the coils are tilted to form a 90° angle (Fig. 3), and distanced by 5 cm over the x-axis, the magnetic coupling is null when the coils are perfectly aligned [25]. The centers of the coils are displaced by a distance dy, moving from 0 to 10 cm over the y-axis. For the single square loop, the optimum value of the mutual inductance is obtained for a dy misalignment of 3.5 cm, i.e. under the wire, which generates a magnetic field around the wire. The optimum value is almost divided by 3 compared to the TAG parallel configuration.

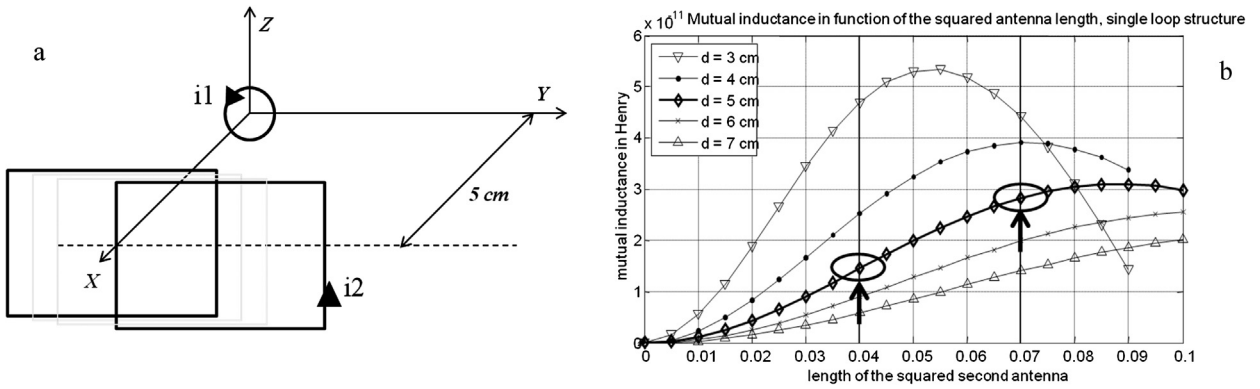

Fig. 2. Distance d in the TAG parallel configuration: a) square loop for the reader coil and circular loop for the TAG; b) Mutual inductance versus the length of the square loop.

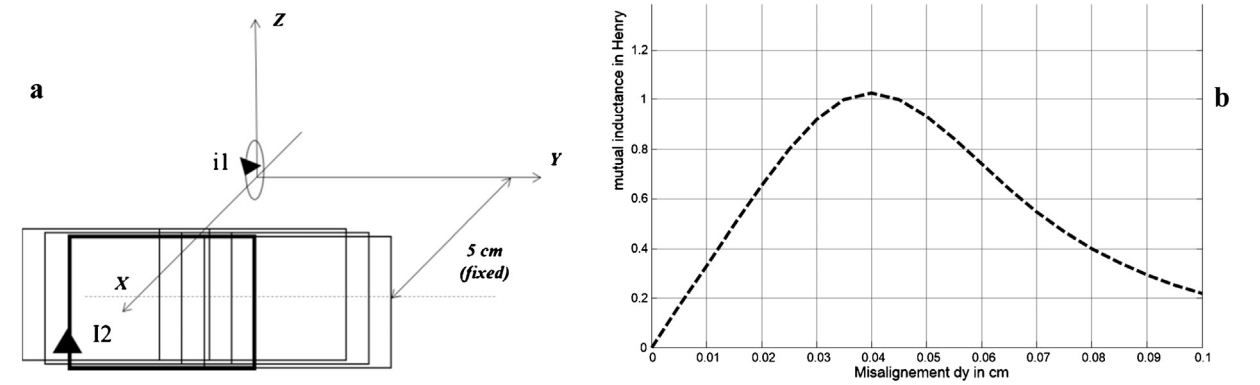

Fig. 3. Misalignment dy in the TAG normal configuration; a) square loop for the reader coil and circular loop for the TAG; b) mutual inductance versus the dy misalignment.

3.3. TAG orientation and position versus the center of the reader's plane

The general case, where both lateral and angular misalignments of the capsule are present, is considered in HL (horizontal link in Fig. 4a) and in VL (vertical link in Fig. 4b) configurations for RX square loops with the previous TX circular loop. We report $10\,\mathrm{Log}_{10}(M)$ versus the angular misalignment dθ for different lateral misalignments dy in parallel and orthogonal configuration for the RX square loop (4 cm × 4 cm and 7 cm × 7 cm) and the TX circular loop. As S_{21} is proportional to M^2 according to (3) and (7), the comparison between the mutual inductance and the simulated or measured $\mathrm{Log}_{10}(S_{21})$ is more easily made. In order to limit the data processing, the studied dθ range is comprised only in the range between 0 and ±90°, where interesting phenomena are observed. It is important to note that the evolution of $\mathrm{Log}_{10}(M)$ versus the [±90°; 0°] range is not symmetrical: there is only a symmetry for the lateral misalignment d$y = 0$ cm.

Both configurations could be associated with each other in an array to guarantee an effective mutual inductance.

For HL (solid line), the mutual inductance is optimum versus the lateral misalignment dy (in cm) and the angular misalignment dθ (in degrees). For instance, with a 4 cm × 4 cm loop and in the [0°; 90°] range (Fig. 5), the mutual inductance, versus the angular rotation at a distance d$x = 5$ cm and a misalignment dy from 0 to 3 cm, is maximum for (dy, dθ) equal to (0, 50°); (1, 35°); (2, 30°); (3, 20°), and minimum for (0, 90°); (1, +75°); (2, 59°); (3, 44°).

For HL (solid line) and VL (dotted line) in the [−90°; 0°] range with a 7 cm × 7 cm loop (Fig. 6), the mutual inductance versus the angular rotation at distance d$x = 5$ cm and the misalignment dy from 0 to 3 cm is optimum versus the lateral misalignment dy (in cm) and angular misalignment dθ (in degree): the mutual inductance in HL is maximum for (dy, dθ) equal to (0, −45°); (1, −54°); (2, −64°); (3, −70°) and minimum in VL for (0, 0°); (1, −9°); (2, −18°); (3, −26°).

When the length L of the RX square coil increases from 4 cm to 7 cm in HL (solid line) and VL (dotted line) configurations (Fig. 7), the maximum value of mutual inductance, versus the angular rotation at distance d$x = 5$ cm and misalignment d$y = 3$ cm, is higher, and the minimum of M is obtained when the angle dθ decreases. The length L, increasing from 4 cm to 7 cm, multiplies the mutual inductance by 2.15 when the coils are co-axial (Fig. 2b), which corresponds to $10\,\mathrm{Log}_{10}(M) =$ 3.3 dB. To avoid VL configuration and assure the compactness of RX array, it seems easier to fabricate an RX prototype with a length of 7 cm.

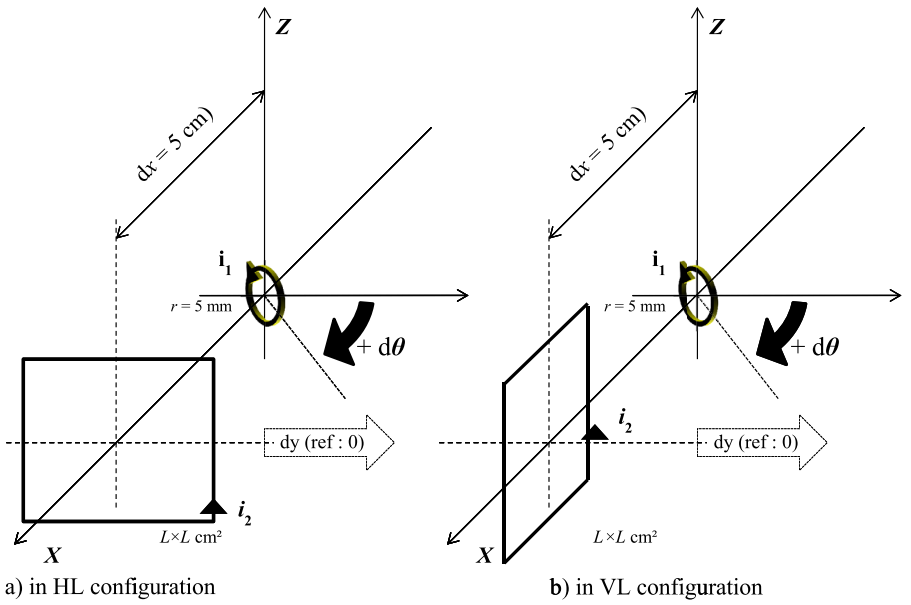

Fig. 4. HF and VL configurations.

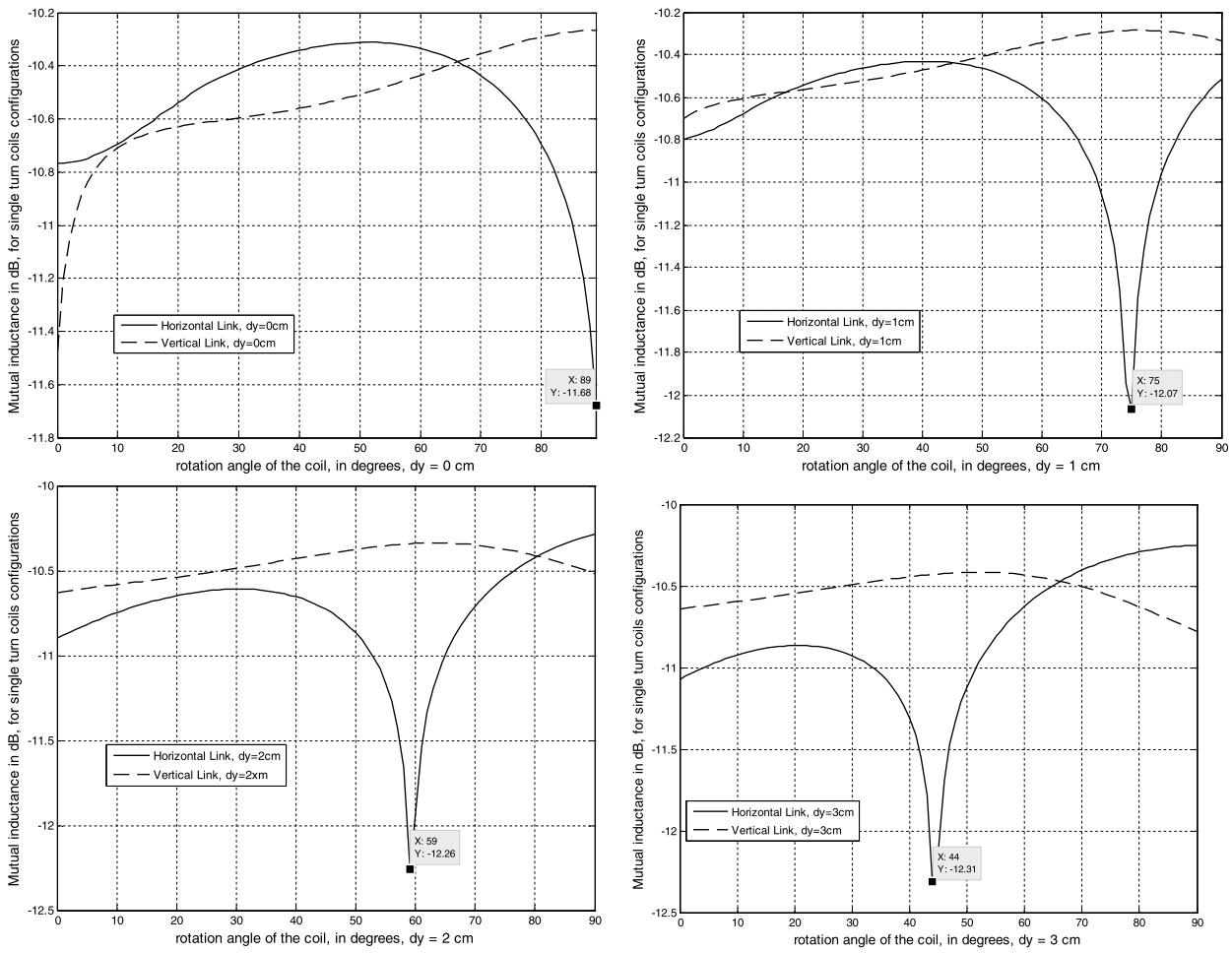

Fig. 5. Mutual inductance in HL (solid line) and VL (dotted line) configuration (4 cm × 4 cm square loop).

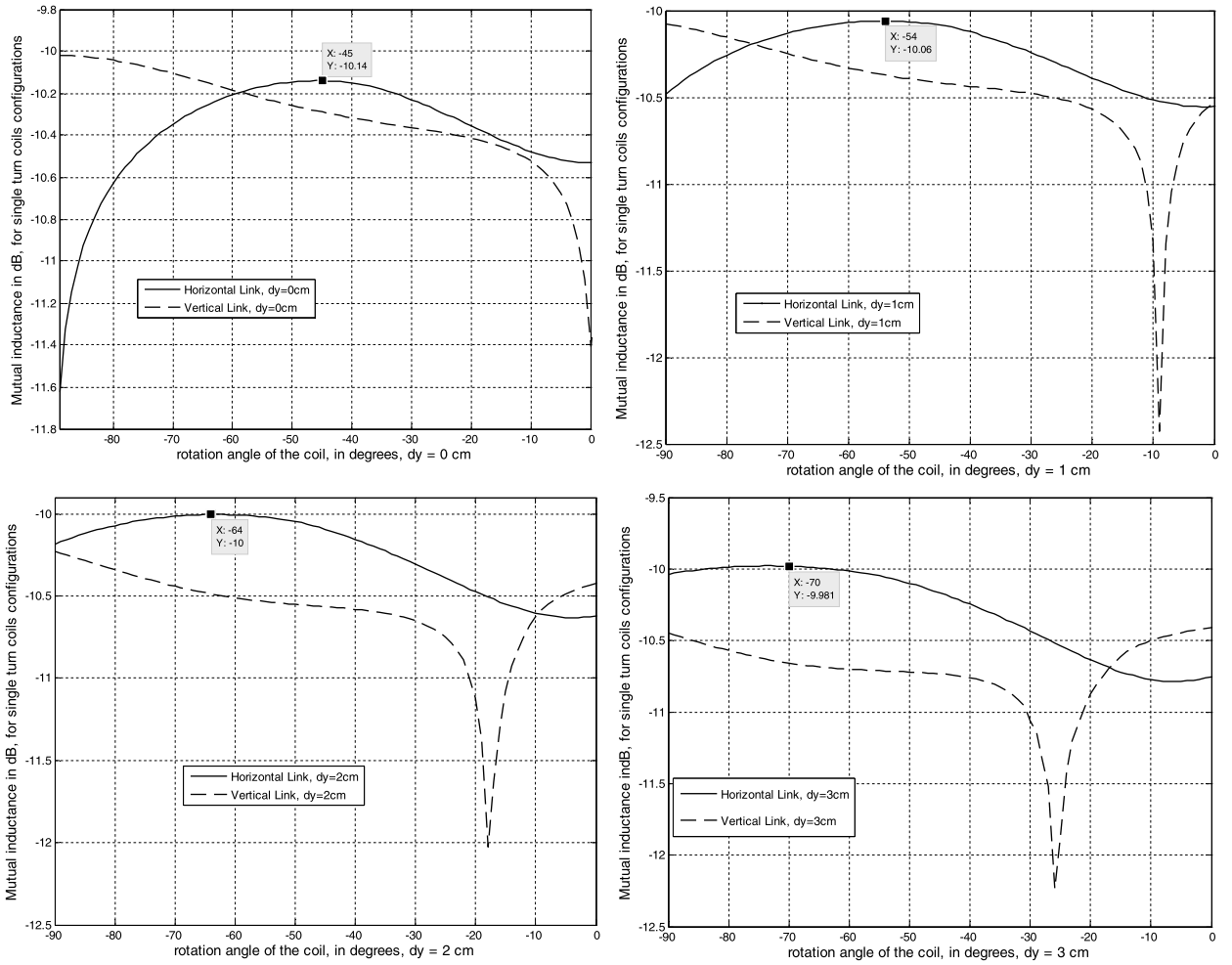

Fig. 6. Mutual inductance in HL (solid line) and VL (dotted line) configuration (7 cm × 7 cm square loop).

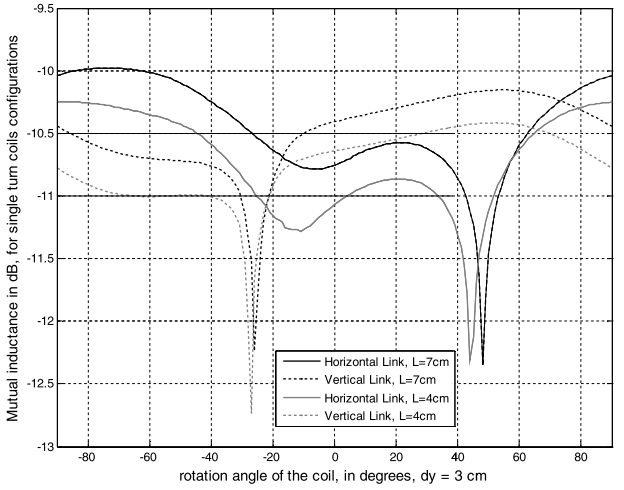

Fig. 7. Mutual inductance in HL (solid line) and VL (dotted line) configuration for $L = 4$ cm and 7 cm.

In the following section, the design of the coils and the inductive link was carried out using HFSS (High-Frequency Structural Simulator) [28], which is a commercial full-wave software based on the Finite-Element Method to evaluate the inductive link performances through the human body and the air.

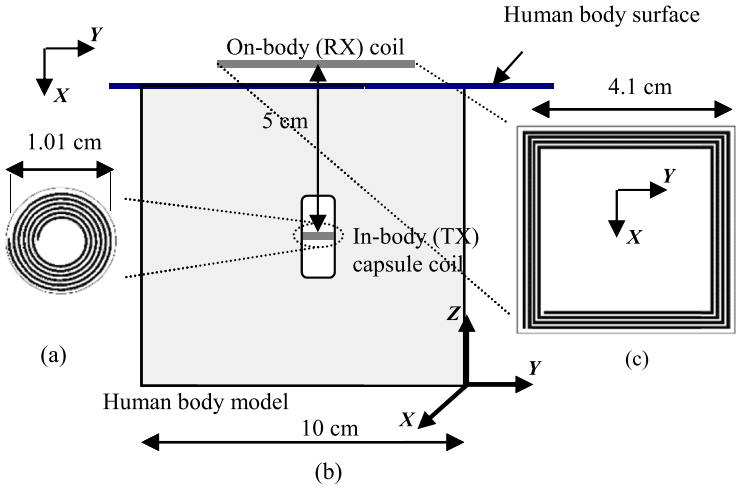

Fig. 8. (a) Spiral coil TX antenna geometry (antenna 1); (b) MI link through the homogeneous human body; (c) square coil RX antenna geometry (antenna 2).

Table 2
Characteristics of the simulated antennas in the presence of the human body and in the air at 40.68 MHz.

Antenna characteristics	R_{LT} (Ω)	R_{LR} (Ω)	X_{LT} (Ω)	X_{LR} (Ω)	L_T (μH)	L_R (μH)	Q_T	Q_R	η_T	η_R	k
Human body ($\varepsilon_r = 83$; $\sigma = 0.67$ S/m)	0.8	7	74.5	514	0.3	2	1.5	9	0.98	0.88	0.04
Air ($\varepsilon_r = 1$; $\sigma = 0$ S/m)	0.8	4	74.5	512	0.3	2	1.5	9.5	0.98	0.92	0.05

4. Monolayer coil for TX capsule: simulated MI characteristics

In this study, the length of the square coil can be considered equal to 4 cm, to be compared with the previous study (in Fig. 2) in the parallel TAG configuration. The capsule diameter is of the same order as that of the circular coil.

4.1. Simulated characteristics and electrical equivalent model

Given the dielectric parameters ($\varepsilon_r = 83$ and $\sigma = 0.67$ S/m at 40.68 MHz) of the average human muscle, the transmission parameter is investigated in two different media, air and human muscle in a $10 \times 10 \times 10$ cm^3 cubic box as illustrated in Fig. 8b. The in-body transmitter capsule coil [30] is inserted into a cylinder having the size of a vitamin pill filled with air. The capsule is placed at the center of the cubic box: it consists of a 6-turn coil, with an outer diameter of 10.1 mm, and line width and space between the lines equal respectively to 0.25 mm and 0.2 mm, as depicted in Fig. 8a. The on-body coil is positioned coaxially with the in-body coil at 5 cm beneath the side of the cubic box (Fig. 8b). As shown in Fig. 8c, the dimensions of the four-turn on-body antenna are $41 \times 41 \times 1.5$ mm^3, with a line width and spacing between lines of 0.3 mm. Rogers RT/duroid 5880 substrate ($\varepsilon_r = 2.2$; $\tan\delta = 0.0009$) is used to design both the in-body and the on-body antennas.

A matching system, composed of two capacitors, is designed for each coil to match the coil impedances close to 50 Ω, when the coils are considered separately. According to (3), the empirical transmission S_{21} can be expressed from Q_T, Q_R, η_T, η_R and k. The resistances R_S and R_L are set to 50 Ω and P_T to 1 W. R_{LT}, R_{LR}, L_T and L_R are deduced from the simulated results of the TX and RX coils. From Table 2, the modification of the media affects the RX coil resistance R_{LR}.

The empirical transmission coefficient is calculated using equation (7) for the coupling coefficient, in which the values of inductances are extracted from the simulation using Z_{ij} parameters and is updated in (9):

$$k = \frac{\mathrm{Im}(Z_{12})}{\sqrt{\mathrm{Im}(Z_{11}) \times \mathrm{Im}(Z_{22})}} \tag{9}$$

where port 1 feeds the TX coil and the received power of the RX coil is evaluated at port 2. Z_{11}, Z_{22} and Z_{12} are the impedances of the TX coil, RX coil and the mutual impedance between both coils, respectively. The imaginary parts of Z_{11}, Z_{22} and Z_{12} correspond respectively to the self-inductance of the RX coil, of the TX coil, and to the mutual inductance between both coils. The coupling coefficient is equal to 0.04 in the human body and 0.05 in the air. The low values of k are essentially due to the small dimensions of the coils, particularly the TX capsule coil. From Table 3, we can conclude that the empirical values are not in a good agreement with the simulated results. Nevertheless, the modification of the media affects the inductive link because of the increase of the RX on-body spiral coil resistance, in the presence of the human body. The previous simulations are performed in the homogeneous human body. We have to perform some of them in a multilayer human body model, in order to evaluate the impact on the MI link.

Table 3
Comparison between the coupling response found by empirical formula and HFSS simulation in the human body and in the air around 40.68 MHz.

	Human body	Air
S_{21} empirical (dB)	−17.3	−15
S_{21} simulation HFSS (dB)	−22.1	−20.7

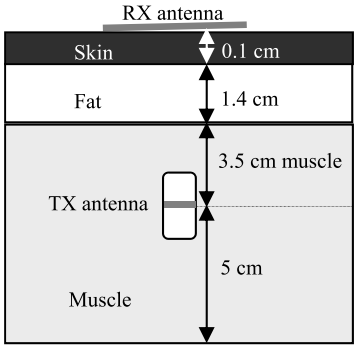

Fig. 9. MI link through a three-layer human body (muscle/fat/skin).

Table 4
Dielectric properties of human tissues employed in the three-layer human body at 40.68 MHz and RF attenuation (dB/cm).

Human tissue	Relative permittivity	Conductivity (S/m)	α (dB/cm)
Muscle	82.6	0.67	0.78
Fat	7.3	0.034	0.16
Skin	124.3	0.38	0.48

Table 5
S_{21} parameter of the inductive links through the air, the three-layer human body and the homogeneous model at 40.68 MHz.

	Air	Three-layer model	Homogeneous model
S21 (dB)	−20.7	−21.1	−22.1

4.2. More realistic model: 3-layer human body and batteries

A three-layer human body is represented in Fig. 9. The dielectric properties of each layer and attenuation α calculated thanks to formula (1) are reported in Table 4. The very low conductivity of fat is close to that of the free-space, which reduces the dissipated energy by the lossy media. By considering the thickness and attenuation of each layer, the 3-layer human body improves by 0.9 dB the medium losses; the field magnitude is improved from 3.92 dB with a muscle to 3.02 dB.

According to Table 5, the inductive link can be improved in the three-layer human body, which is a more realistic model, in comparison with the homogeneous human body. By taking into account the tissue's thickness and attenuation, the discrepancy of almost 1 dB between the three-layer model and the homogeneous one is verified with the attenuation formula (1) and with the S21 parameter (Table 5): the losses are proportional to the volume and the conductivity of body tissues.

The ingestible capsule is powered by a two coin-shaped silver-oxide battery, which can generate 20 mW. The maximum specific absorption rate (SAR) of the human body is recommended under the basic restriction of 0.4 W/kg, averaged over the whole body, by the International Commission of Non-Ionizing Radiation Protection (ICNIRP) [31]. So the SAR value respects the standards.

The measurement of body temperature by an ingestible sensor [9], fed by two silver-oxide batteries, at 40.68 MHz, has been investigated. The receiver was placed less than 50 cm away from the transmitter, the data transmitted every 15 s with a data rate of 80 bps and a battery life of 10 days.

The volume allocated to the batteries is filled with a metallic material. A copper cylinder is included in the TX ingestible capsule to mimic the presence of the power supply. In the worst case, i.e. when the medium is the homogeneous human body, a copper battery ($\mu_r = 0.99$ et $\sigma = 58 \cdot 10^8$ S/m), whose diameter and thickness are about 10.5 mm and 4 mm, respectively, is placed 3 mm away from the coil substrate. The transmission parameter is reduced by 0.5 dB. To conclude, the performances confirm the adequate coil design and the batteries affect slightly the inductive link.

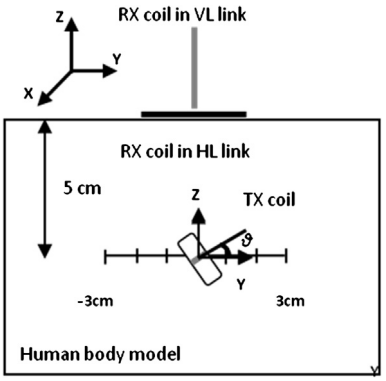

Fig. 10. TX coil angle and position variation according to the OY axis in the HL and VL.

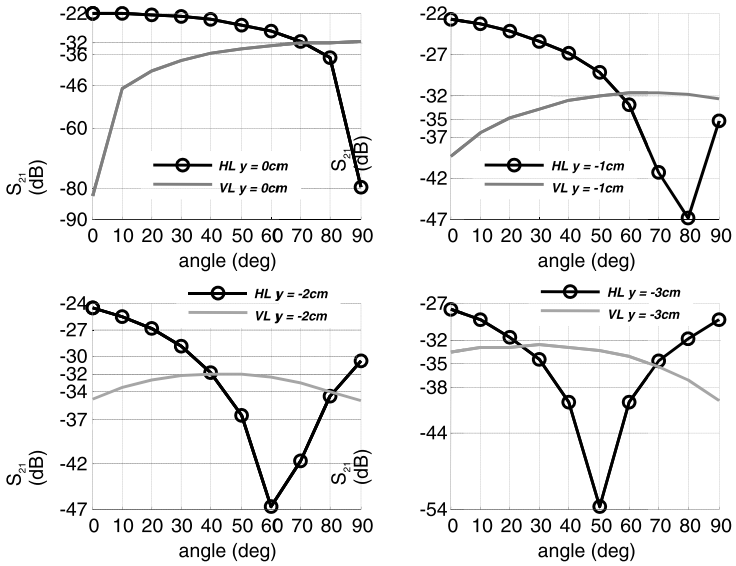

Fig. 11. Simulated transmission parameter at different TX antenna y-positions as a function of the angle θ at 40.68 MHz in the HL and in the VL.

4.3. With a RX-coil array

The ingestible capsule slides down into the gastro-intestinal (GI), so the relative position and orientation of the TX coil versus the RX spiral coil must be taken into account to evaluate the inductive link. The TX coil orientation is reported as a function of the angle θ, $\theta = 0°$ corresponding to the horizontal link (HL link) and $\theta = 90°$ to the vertical link (VL link) and the TX coil position is referenced by the OY axis (Fig. 10). The relative position is defined as the spacing between the capsule coil and the spiral coil in the y-direction. The transmission parameters of the HL and VL links have been performed separately. Another possibility is to realize a multi-coil capsule. Three coils, which are geometrically orthogonal to one another, are inserted in the capsule to ensure an adequate coupling with the reader coil [11].

For each relative position, comprised between -3 cm and 3 cm, the inductive link's efficiency at 40.68 MHz is acceptable for any coil angle orientation, subject to considering both complementary VL and HL links. In fact, while the TX capsule coil slides in the GI tract, the RX-received power can be optimized by the position and the orientation. The evolution of the S_{21} parameter according to the angle in different y-positions at 40.68 MHz is depicted in the four sub-plots of Fig. 11, where every portion corresponds to a TX antenna y-position ($y = 0, -1, -2$ and -3 cm). We can conclude from these plots that for all selected y-positions, the maximum occurs when $\theta = 0°$. This configuration represents the optimum position where there are maximum H-field lines perpendicular to the on-body antenna surface. Over the dθ variation range [0°; 90°], the behavior of $10\,\mathrm{Log}_{10} S_{21}$ (Fig. 11) is almost similar to the $\mathrm{Log}_{10}(M)$ function (Fig. 5), which is optimum versus the angular variation: in the HL configuration, the angle, where the minimum value is obtained, decreases according to the dx misalignment rise, but the maximum is always obtained in simulation when dθ is equal to zero, while the curve profile is different under MATLAB, where the angular position, allowing one to obtain a maximum level of mutual inductance, changes and depends on the lateral misalignment (Fig. 5). The optimum angles are slightly different under HFSS simulation and MATLAB analysis, probably because of the multi-turn structure in simulation and the one-turn coil under MATLAB for

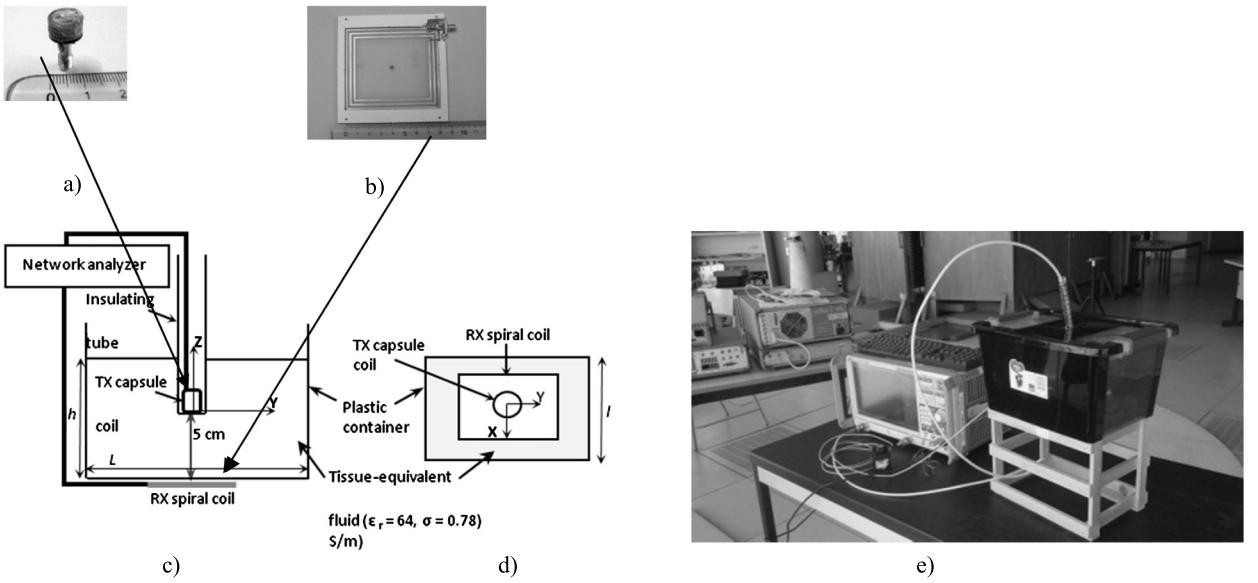

Fig. 12. (a) Fabricated TX multilayer capsule coil; (b) fabricated RX 3-turn receiver spiral coil; measurement set-up: (c) side view; (d) top view; (e) pictures of the measurement set-up.

Table 6
Capacitances values of the transmitter and the receiver antennas, when the transmission channel is either the human body or the air.

		Series capacitance (pF)	Parallel capacitance (pF)
In free-space	TX coil	180	800
	RX coil	8.2	213
In the human body	TX coil	180	800
	RX coil	7.6	56

the TX and RX coils and also because of the different media: we considered air ($\varepsilon_r = 1$; $\sigma = 0$ S/m) as the medium on MATLAB and the human body ($\varepsilon_r = 83$; $\sigma = 0.67$ S/m) for simulated results.

Due to the non-compactness of the RX array, with the coils oriented perpendicularly to the surface, we propose to increase the dimensions of the RX coils from 4 cm to 7 cm (to increase the mutual inductance, like reported in Fig. 6) and the layers of the TX capsule coil. To perceive dissimilarities, the fabricated prototypes will be positioned in an human-tissue-equivalent fluid.

5. Multilayer coil for the TX coil: simulation and measurement

In this study, the length of the square coil can be considered to be between 7 cm and 8 cm in the theoretical study on the mutual inductance (in Fig. 2) for the TAG parallel configuration. The capsule diameter is of the same order as that of the circular coil.

5.1. Realized TX and RX coils and measurement setup

To increase the magnetic field's strength, the TX capsule coil is chosen as a five-layer coil and the RX coil surface increases from 4.1 cm × 4.1 cm to 7 cm × 8 cm [32]. The advantages of the multilayer printed coil compared to the classic wired coil are essentially the robustness and the solidity. The structure of the capsule antenna (Fig. 12a) consists of five different loops, which lie on different layers of FR4 epoxy with a dielectric constant ε_r of 4.4, a dielectric loss tangent of 0.02 and a metallic thickness of 35 μm using mechanical etching, separated by four FR4 super-strata with a thickness of 0.76 mm to ensure both a stable distance between the coil turns and a more solid structure. The inner and outer radii of the loops are respectively 8.5 mm and 9.5 mm. Each loop has two circular catch pads 0.7 mm in diameter, which are used to connect the metal via loops. In order to increase the received power through the inductive link, the on-body receiver coil needs to have large dimensions, as illustrated in Fig. 2. As shown in Fig. 12(b), the dimensions of the three-turn on body antenna on FR4 substrate are $70 \times 80 \times 0.76$ mm^3, with a line width and spacing between lines of 1.5 mm.

The L-matching circuit (Fig. 1), using lumped capacitances (Table 6), has to be adjusted to match the impedance from the source (R_S) to the TX coil (L_T, R_{LT}) and from the RX coil (L_R, R_{LR}) to the load (R_L) and when the MI link is established.

Table 7
Simulated and measured coil characteristics in the presence of the human body and in air at 40.68 MHz.

Antenna characteristics	R_{LT} (Ω) in the human body	R_{LR} (Ω)	L_T (μH)	L_R (μH)	Q_T	Q_R	η_T	η_R	k
Simulation in phantom	0.32	14.2	0.12	1.7	0.6	6.7	0.99	0.78	0.11
Measurement in phantom	0.52	26.8	0.12	2.1	0.61	7.1	0.99	0.65	
Simulation in air	0.3	2.4	0.12	1.6	0.6	8	0.99	0.95	0.22
Measurement in air	0.57	5.1	0.12	2	0.61	9.1	0.99	0.91	

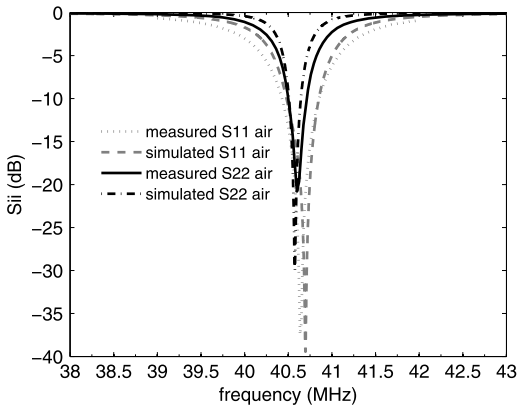

Fig. 13. Simulated and measured reflection coefficients of the transmitter (S_{11}) and the receiver (S_{22}) coils in the air.

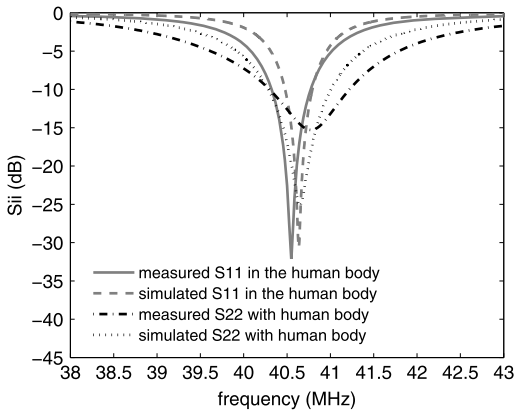

Fig. 14. Simulated and measured reflection coefficients of the transmitter (S_{11}) and the receiver (S_{22}) coils through the human body.

The coils were measured by using a homogeneous human-tissue-equivalent fluid available in our laboratory, whose dielectric properties ($\varepsilon_r = 64$ and $\sigma = 0.78$ S/m) are extrapolated from the measured curve with the Agilent Dielectric Probe Kit (200 MHz–20 GHz) and are taken into account in the simulation to evaluate the inductive link performances. The in-vitro measurement was carried out by Rohde Schwarz ZNB8, as shown in Fig. 12c–e. The TX coil is placed in the rectangular box with dimensions 29.2 cm × 22.2 cm × 16.5 cm (L, l, h) at $h = 5$ cm, which is higher than the RX external coil, whose spacing of 0.4 cm is comprised of air, to take into account the air gap between the receiver coil and the back side of the rectangular box needed to insert the SMA connector. The capsule antenna is isolated from the body liquid by a Plexiglas tube, whose diameter and thickness are respectively equal to 1.4 cm and 0.5 mm [32]. A ferrite core is applied to the feeding coaxial cable, which is connected with the RX coil and to the network analyzer to prevent disturbance currents from flowing in the cable.

5.2. Coil characteristics, matching and transmission

Extracted electrical circuits deduced from simulated and measured input impedances of TX and RX coils, when the media is human body and air, are listed in Table 7. The impedance (Table 7) and the measured bandwidth (Figs. 13 and 14) of the RX coil impedance decrease, when the transmission channel changes from the human body to the air. The TX coil seems less sensitive to the media variation, because of its insertion in the Plexiglas tube filled with air: the −10 dB matching bandwidth is equal to 1% (around 0.47 MHz) in the air and in the human body. We also analyze the coupling efficiency

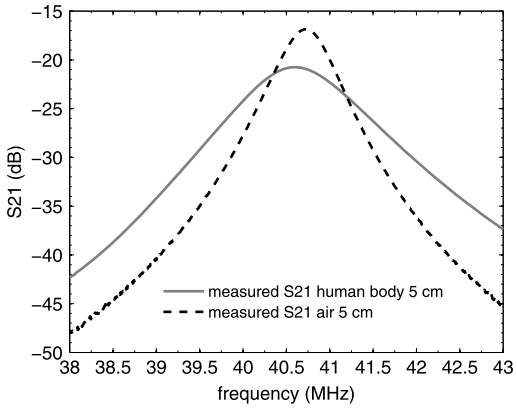

Fig. 15. Measured coupling response S_{21}, according to the frequency, between the capsule coil and the receiver coil separated by a distance of 5 cm when the path is the human body and the air.

Table 8
Comparison between the coupling response found by empirical formula, HFSS simulation, measurements and ADS simulation in different medias around 40.68 MHz.

	S_{21} empirical	S_{21} simulation (HFSS)	S_{21} measurements	S_{21} simulation (ADS)
Human body ($\varepsilon_r = 64;\ \sigma = 0.78$ S/m)	−14.2 dB	−18.1 dB	−20.7 dB	−15.9 dB
Air ($\varepsilon_r = 1;\ \sigma = 0$)	−6.6 dB	−10.5 dB	−16.8 dB	−21.3 dB
"Non-conductive" human body ($\varepsilon_r = 64;\ \sigma = 0$ S/m)	Ø	−10.4 dB	Ø	Ø

in the human body and in the air at 40.68 MHz with an empirical formula based on the Agbinya–Masihpour model [24], with HFSS electromagnetic simulation, ADS electrical circuit simulation and measurement. Moreover, the efficiency of the inductive link in measurement, represented by the S_{21} parameter, can reach 0.85% (−20.7 dB) in the human body.

The following paragraphs discuss the lack of accuracy in the measurement of the characteristics of the human-tissue-equivalent fluid, the attenuation introduced by the media, by mismatching the connection between the load (or the source) represented in the experimental part by the cable and the RX coil (or TX coil), by conductor losses and by the ferrite core encircling the cable.

The dielectric properties ($\varepsilon_r = 64$ and $\sigma = 0.78$ S/m) of the homogeneous human-tissue-equivalent fluid are extrapolated from measurement in the 200 MHz–50 GHz band with the Agilent Dielectric Probe Kit. As transmission attenuation depends on the square root of the conductivity, the lack of accuracy in the measurement of the complex permittivity can result in discrepancies between simulation and measurement.

To evaluate the influence of the dissipative media on the received power obtained by magnetic coupling, we plot the measured coupling response when the channel is the human body and the air in Fig. 15. As it is depicted by these plots and in Table 8, the coupling response in the air and in the human body at 40.68 MHz is equal to 7.6 dB in the HFSS simulation and with empirical formula (3), 3.9 dB in measurement, while media losses are calculated at 4.04 dB in the beginning of paragraph 2. An overcoupling in the air is observed with the electrical circuit simulation and deteriorates the transmission parameter to −21.3 dB at 40.68 MHz. As it is seen in Table 8, the media attenuation depends essentially on its conductivity: the modification of the relative permittivity from 1 to 64 does not affect the efficiency coupling in air and in the "non-conductive" human body. The measured frequency shift of TX and RX coils with air and with human body media (Figs. 13 and 14) can explain the fact that the measured MI link is less effective than the simulated one. The critical factor seems to be the L-matching circuit, made of lumped capacitors. We focus on the serial resistance and relative value of this capacitor.

The reactance X of the capacitors is comprised between 0.002 Ω and 0.2 Ω for capacitor values varying from 7.6 pF to 800 pF at 40.68 MHz. To evaluate the impact on the power transfer with the capacitor circuits in the human body, a high serial resistance of 0.2 Ω is associated with both capacitors in TX and RX coils, and the S_{21} parameter is reduced from −15.9 dB to −16.2 dB. A ± 5% variation on the capacitors with zero serial resistance affects the coupling efficiency of ±1 dB. However, this S_{21} range, with the relative error on the capacitor and the serial resistance, stays less than the measured one, but can contribute to increase the discrepancies between simulation and measurement.

In order to qualify the effect of the conductor loss composed of skin-effect loss, proximity-effect loss and DC conduction loss, copper lines in the RX and TX coils are replaced by a Perfect Electric Conductor (PEC). As the signal transmission is improved from −18.1 dB to −12.4 dB with TX coil mismatching, there are conductor losses, which cannot be neglected in the simulation. In particular, the size of the meshing cells in the conductor has to be less than 10 µm of skin thickness.

The measurement of a small coil requires the connection with a coaxial cable, that disrupts the impedance of the coil, due to current on the outer surface of the cable. Baluns of ferrite [33] for EMI (Electromagnetic Interference) suppression [34,35] have been added on the outer surface, but they limit the frequency band and the efficiency. Sometimes, in radia-

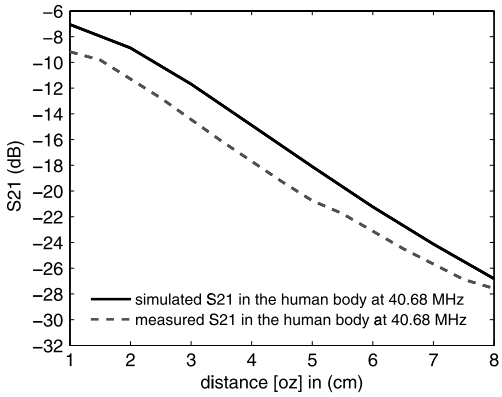

Fig. 16. Simulated and measured coupling response S_{21} according to the z-distance around 40.68 MHz in the human body.

tive emission, the use of an electro-optical transducer and a fibre link, associated with the post-processing step [36], are investigated to avoid the use of an RF cable [37]. A method for explaining the discrepancy between the simulation and the measurement requires two different measurements of the S_{21} parameter with and without a feeding coaxial cable in proximity to the dissipative human body, acting as a metallic plane. The S_{21} level is comparable without cable and with cable and de-embedding: a level shift of 0.2 dB on the S_{21} with and without cable is obtained after optimization of the capacitor. The measurement is done in the referenced plane of the RX and TX coils input with SOL (Short Open Load) calibration when the RX coil is used with ferrite encircling the cable.

It may be concluded that investigations on the discrepancies between simulation and measurement demonstrated that the L-matching circuit, the approximate dielectric characterization of the media, and the conductor losses were critical factors.

5.3. Distance effects

In the previous section, the TX capsule coil is off-centered by 5 cm away from the RX on-body coil. In this paragraph, the off-center distance varies from 1 cm to 8 cm in the homogeneous human body. Simulated and measured transmission parameters S_{21} versus the off-center distance are reported in Fig. 16. A marginal drop from 1 dB to 2.6 dB is observed between the simulated and measured S_{21}, the slope is almost 10 dB/octave and does not agree with the B-field attenuation function of d^{-3} (power attenuation of 18 dB/octave). B-field attenuation depends on d^{-3} when the radius of the coils is inferior to the distance between the coils: the radius, equal to 0.5 cm and 4.22 cm (calculated radius from the equivalent surface) for the TX and RX coils are in the same order than the distance of 5 cm and formula (4), entailing the size of the coils and the distance between coils, cannot be applied. The discrepancies between simulation and measurement are due to the L-matching circuit (Fig. 1), with a frequency shift, the value of capacitance not being optimized for each distance.

5.4. Angular and misalignment effects

In this study, the TX capsule coil is 5 cm away from the RX coil. A homogeneous rectangular cuboid human body with a smaller height, i.e. with dimensions of 38.5 cm × 33 cm × 8 cm (L, l, h) is considered as allowing a maximum variation of the angle, but it is not possible to reach the 90° angle: a measurement setup is realized to avoid the mechanical shift between the coils and, in this configuration, the tissue-equivalent fluid could flow into the isolated tube in the 90° angle orientation (Fig. 17). Simulated and measured transmission coefficients for the four positions (y-positions equal to 0, 1, 2 and 3 cm) are depicted in Fig. 18. The measurement is always worse than the simulation, but the maximized transmission parameter versus the angle is obtained in simulation when the coils are coaxially positioned, while the angle is shifted from 0 to −26° when the coils are misaligned from 0 cm to 3 cm, if we consider that dθ in MATLAB corresponds to −dθ in the experimental part: the behavior is similar to the mutual inductance variation, which is maximum in Fig. 6 for the angular rise when the dx misalignment position becomes greater. The angle, where the maximum is effective, is slightly different under HFSS simulation and MATLAB analysis, because of the multilayer structure (each loop can be equivalent to a loop with a different diameter for a constant distance) for the RX coils and different propagating media. The measurement accuracy errors can be increased with the previous part because of a mechanical shift on the y-position and on the angle.

To conclude, for every capsule antenna position, a coupling response is calculated versus the angle increase: the S_{21} response varies between −20.5 dB and −35.5 dB. If we consider that for a −32 dB response the MI link is effective, the configuration for y-position = 0 cm and $\theta = 80°$ can be considered like a limit. Moreover, to avoid low coupling response in some capsule orientations, a fabricated prototype with metalized holes allowing a turn number increment and manufacturing facilities for the same total TX coil height would be an advantage.

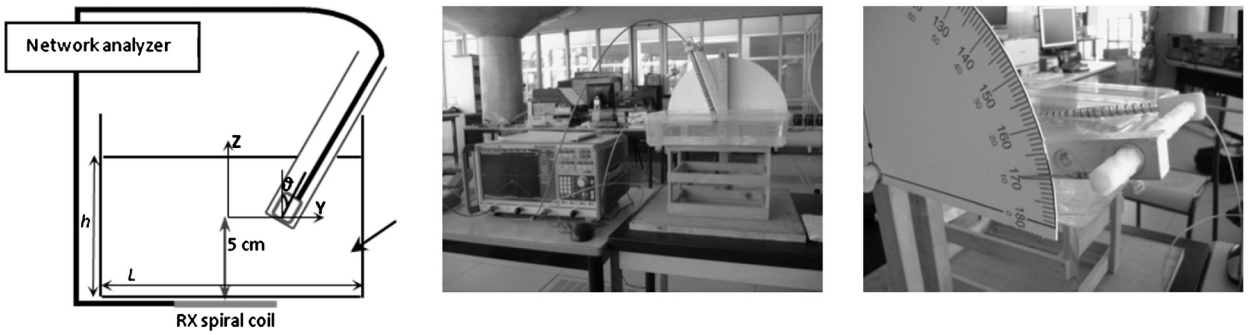

Fig. 17. Measurements set-up when the position and the orientation of the capsule antenna change: (a) side view; (b), (c) pictures of the measurement-setup.

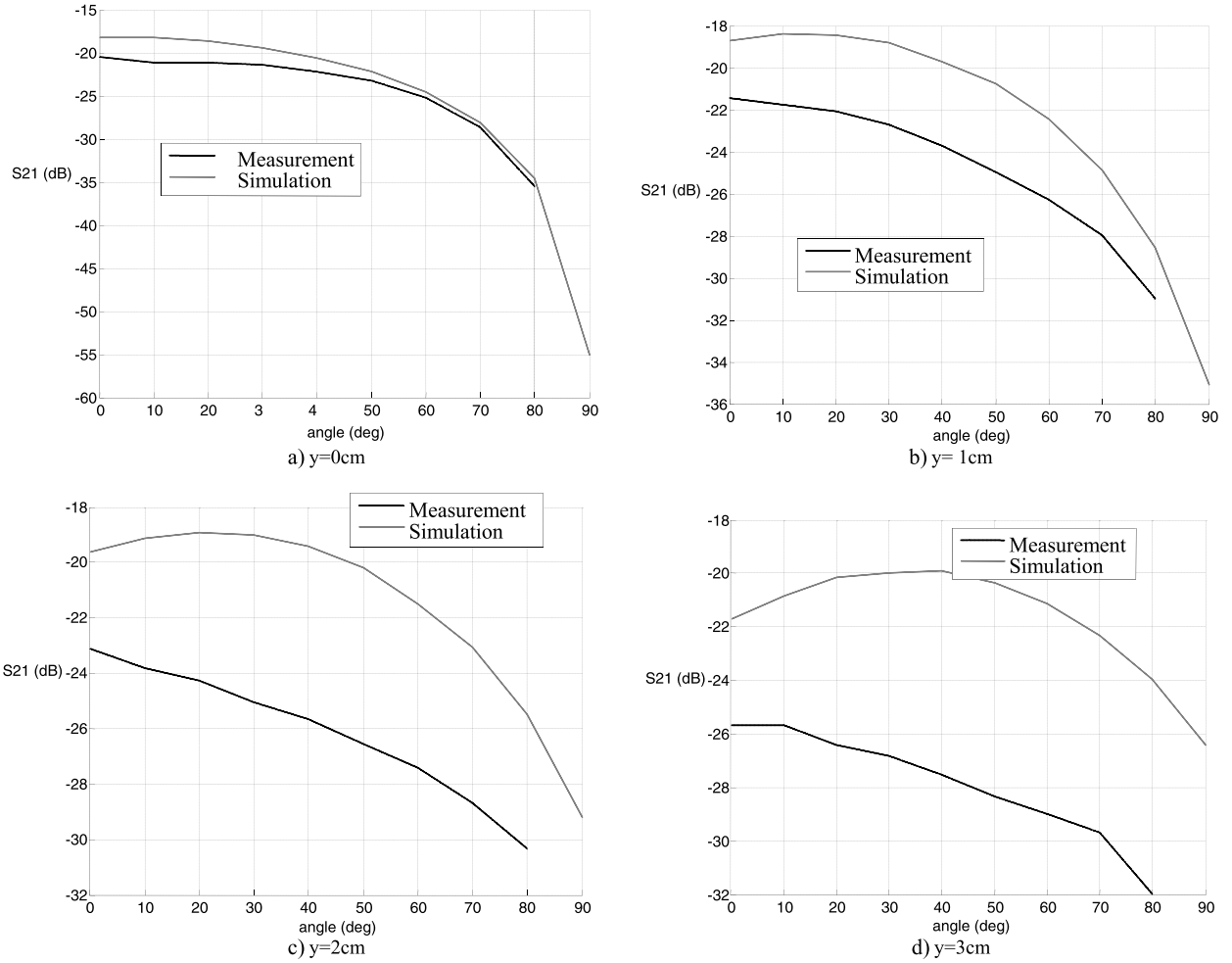

Fig. 18. Simulated and measured coupling response S_{21} around 40.68 MHz in the tissue-simulating fluid according to the angle at different y-positions.

6. Conclusion

For wireless ingestible capsule systems, modelling and optimization of the complete transmission link in the presence of the human body is necessary. The FEM method is used to model the MI link, which is carried out using HFSS, a commercially-available FEM piece of software. To capture the behavior of the MI in wireless ingestible capsule, the TX coil is inserted in a capsule, surrounded by a human body. To represent the body properties in numerical modelling, we consider a homogeneous and a three-layer model. In measurement, we employ a human tissue-equivalent fluid, whose

dielectric properties are characterized by a dielectric probe kit. The MI link is evaluated by taking into account the relative position and orientation of the TX coil versus the RX coil. Multiple (ideally orthogonal) loops could be used to avoid coupling minima attributable to the TX coil orientation.

The results discussed in this work are:

(1) analysis of the coil impedance and loaded quality factor,
(2) mutual inductance between one-turn circular and square coils versus the lateral and angular misalignment,
(3) analytical, simulated, measured MI link budget and electrical circuit simulation,
(4) observation of the received relative signal response versus the angular and misalignment of capsule's coil in the small intestine,
(5) consideration of two MI links
  – a TX monolayer coil and a RX 4.1 cm × 4.1 cm coil-orthogonal array
  – a TX multilayer coil ($\phi \times h = 9.5$ mm × 2 mm ($0.0013\lambda_o \times 0.0003\lambda_o$)) and a RX 7 cm × 8 cm coil.

To conclude, the efficiency of the MI link as a function of various environmental and coupling conditions is established and experimentally demonstrated. If we compare the simulated results for the first (Fig. 11) and the second coil structures (Fig. 18), we can notice an improved value of S_{21} due to the RX coil size increase, despite the medium conductivity rise between simulation and measurement (from 0.67 S/m to 0.78 S/m): in the simulation, the S_{21} previously comprised between −22 and −80 dB for a 4 cm × 4 cm loop is increased to −18.1 to −50 dB for a 7 cm × 8 cm loop. For co-axial coils in HL configuration, the 3.9-dB maximum level enhancement, which varies from −22 to −18.1 dB, is in agreement with the theoretical part, where L increases from 4 cm to 7 cm (the coil is assimilated to a square, but it is a rectangle) multiplies the mutual inductance by 2.15 (Fig. 2b), which corresponds to $10\,\mathrm{Log}_{10}(M)$ equal to 3.3 dB. The efficiency improvement depends on the RX size increasing mainly, but probably also slightly on the TX structure, composed of a 6-turn monolayer coil, and a 5-turn multilayer coil, whose discrepancy regarding the optimization was not evaluated in this paper, focusing on mutual inductance. Simulated investigations on the measurement errors demonstrated that the matching characteristics of the matching network, and the conductor losses were critical factors that controlled measurement accuracy. Lack of accuracy on the dielectric characterization of human body equivalent liquid because of the low frequency limit at 200 MHz of the Probe and the mechanical shift of the in-vitro measurement can bring some errors.

As a perspective, the design of a RX coil array, pressed on the abdomen, to ensure power efficiency for an arbitrary capsule's orientation and to determine the TX coil position in the small intestine should be considered. To identify the zone, where is located the capsule in the small intestine, for instance in order to evaluate the transit time and functional exploration, the position is currently deduced from the changes of PH values, but the low sensitivity of PH sensors and the PH modification with digestive disorders are not accurate. With a cheap wearable system, we could focus on the LF RFID technology to be less sensitive to the medium's conductivity. Capsules, including several sensors, could be swallowed to determine the capsule position: multiple sensors in the wireless ingestible capsule can provide data and data processing allows one to determine more accurately the position of the capsule [39]. In the capsule, an inclinometer [38], an anticollision function could be added to maximize the detection by zone and the battery life time through low power consumption. To avoid battery discharge, some researchers focus on energy harvesting from human body: conversion from body mechanical energy, such as blood flow, breathing… into electrical energy for the implanted devices [40–43]. The losses in the medium are lower as frequency decreases and can be evaluated numerically and experimentally [44]. In future works, the fabrication of a RX belt to identify and localize LF-RFID TAGs in the small intestine should be studied.

References

[1] M. Q-H Meng, et al., Wireless robotic capsule endoscopy: state-of-the-art and challenges, in: Fifth World Congress on Intelligent Control and Automation, WCICA, June 2004, pp. 5561–5565.
[2] Sang Heun Lee, Young Joong Yoon, Fat arm spiral antenna for wideband capsule endoscope systems, in: Radio and Wireless Symposium, RWS, IEEE, Jan 2010, pp. 579–582.
[3] Sang Heun Lee, Jaebok Lee, Young Joong Yoon, Sangbok Park, Changyul Cheon, Kihyun Kim, Sangwook Nam, A wideband spiral antenna for ingestible capsule endoscope systems: experimental results in a human phantom and a pig, IEEE Trans. Biomed. Eng. 58 (6) (2011) 1734–1741.
[4] Yan Guozheng, Huang Biao, Peng Zan, Design of battery-less and real-time telemetry system for gastrointestinal applications, in: IEEE International Conference on Control and Automation, May–June 2007, pp. 245–249.
[5] L. Wang, T.D. Drysdale, D.R.S. Cumming, In situ characterization of two wireless transmission schemes for ingestible capsules, IEEE Trans. Biomed. Eng. 54 (11) (Nov. 2007) 2020–2027.
[6] N. Aydin, T. Arslan, D.R.S. Cumming, Design and implementation of a spread spectrum based communication system for an ingestible capsule, in: 24th Biomedical Engineering Society EMBS/BMES Conference Engineering in Medicine and Biology, vol. 2, 2002, pp. 1773–1774.
[7] Harish Rajagopalan, Yahya Rahmat-Samii, Novel ingestible capsule antenna designs for medical monitoring and diagnostics, in: Proceedings of the Fourth European Conference on Antennas and Propagation, EuCAP, April 2010, pp. 1–5.
[8] H. Rajagopalan, Y. Rahmat-Samii, Ingestible RFID bio-capsule tag design for medical monitoring, in: Proceedings IEEE AP-S/USNC-URSI, July 2010.
[9] K. Yamasuen H. Hagiwara, O. Tochikobo, C. Sugimoto, R. Kohno, Measurement of core body temperature by an ingestible capsule sensor and evaluation of its wireless communication performance, Adv. Biomed. Eng. 1 (1) (2012) 9–15.
[10] H. Rajagopalan, Y. Rahmat-Samii, Link budget analysis and characterization for ingestible capsule antenna, in: International Workshop on Antenna Technology, IWAT, March 2010, pp. 1–4.
[11] W. Xin, G. Yan, W. Wang, Study of a wireless power transmission system for an active capsule endoscope, Int. J. Med. Robot. Comput. Assist. Surg. (2010) 113–122.

[12] M.R. Basar, F. Malek, K.-M. Juni, M. Shaharom Idris, M. Iskandar, M. Saleh, Ingestible wireless capsule technology: a review of development and future indication, Int. J. Antennas Propag. (2012) 1–14.
[13] Z. Jia, G. Yan, H. Liu, Z. Wang, P. Jiang, Y. Shi, The optimization of wireless power transmission: design and realization, Int. J. Med. Robot. Comput. Assist. Surg. (2012) 337–347.
[14] B. Lenaerts, R. Puers, An inductive power link for a wireless endoscope, Biosens. Bioelectron. (2007) 1390–1395.
[15] Chee Wee Kim, T.S.P. See, RF transmission power loss variation with abdominal tissues thicknesses for ingestible source, in: 13th IEEE International Conference on e-Health Networking Applications and Services, Healthcom, 2011, pp. 282–287.
[16] P.M. Izdebski, H. Rajagopalan, Y. Rahmat-Samii, Conformal ingestible capsule antenna: a novel chandelier meandered design, IEEE Trans. Antennas Propag. 57 (4) (2009) 900–909.
[17] Changrong Liu, Yong-Xin Guo, Shaoqiu Xiao, Circularly polarized helical antenna for ism-band ingestible capsule endoscope systems, IEEE Trans. Antennas Propag. 62 (12) (2014) 6027–6039.
[18] Li-Jie Xu, Yong-Xin Guo, Wen Wu, Bandwidth enhancement of an implantable antenna, IEEE Antennas Wirel. Propag. Lett. (2014).
[19] Changrong Liu, Yong-Xin Guo, R. Jegadeesan, Shaoqiu Xiao, In vivo testing of circularly polarized implantable antennas in rats, IEEE Antennas Wirel. Propag. Lett. 14 (2015) 783–786.
[20] R. Carta, G. Tortora, J. Thoné, B. Lenaerts, P. Valdastri, A. Menciassi, P. Dario, R. Puers, Wireless powering for a self-propelled ad steerable endoscopic capsule for stomach inspection, Biosens, Bioelectron. 25 (2009) 845–851.
[21] F. Merli, et al., Design, realization and measurements of a miniature antenna for implantable wireless communication systems, IEEE Trans. Antennas Propag. 59 (10) (2011) 3544–3555.
[22] http://cp.literature.agilent.com/litweb/pdf/5988-3326EN.pdf.
[23] L.S. Xu, M.Q.-H. Meng, Chao Hu, Effects of dielectric values of human body on specific absorption rate following 430, 800, and 1200 MHz RF exposure to ingestible wireless device, IEEE Trans. Inf. Technol. Biomed. 14 (1) (2010) 52–59.
[24] I. Agbinya J, M. Masihpour, Near field magnetic induction communication link budget: Agbinya–Masihpour model, in: Fifth International Conference on Broadband and Biomedical Communications, IB2Com, Dec 2010, pp. 1–6.
[25] K. Finkenseller, RFID Handbook: Radio-Frequency Identification Fundamentals and Application, 2nd edition, Wiley, 2003.
[26] C. Zierhofer, E. Hochmair, Geometric approach for coupling enhancement of magnetically coupled coils, IEEE Trans. Biomed. Eng. (1996) 708–714.
[27] J. Mispelter, M. Lupu, A. Briguet, NMR Probeheads for Biophysical and Biomedial Experiments, Imperial College Press, 2006.
[28] http://www.ansys.com/Products/Simulation+Technology/Electronics/Signal+Integrity/ANSYS+HFSS.
[29] niremf.ifac.cnr.it/docs/DIELECTRIC/AppendixC.html#FF.
[30] F. El Hatmi, M. Grzeskowiak, S. Protat, O. Picon, Link budget of magnetic antennas for ingestible capsule at 40 MHz, Prog. Electromagn. Res. 134 (2013) 111–131.
[31] http://www.icnirp.org/cms/upload/publications/ICNIRPemfgdl.pdf.
[32] F. El Hatmi, M. Grzeskowiak, D. Delcroix, T. Alves, S. Protat, S. Mostarshedi, O. Picon, A multilayered coil antenna for ingestible capsule: near-filed magnetic induction link, IEEE Antennas Wirel. Propag. Lett. 12 (2013) 1118–1121.
[33] C. Icheln, et al., Use of balun chokes in small-antenna radiation measurements, IEEE Trans. Instrum. Meas. 53 (2) (2004) 498–506.
[34] L.J. Foged, et al., Experimental investigation of radiating current distribution and measurement cable interaction on wireless devices, in: EUCAP, 2011, pp. 1585–1588.
[35] J. Urabe, K. Fujii, Y. Dowaki, Y. Jito, Y. Matsumoto, A. Sugiura, A method for measuring the characteristics of an EMI suppression ferrite core, IEEE Trans. Electromagn. Compat. 45 (4) (2006) 774–780.
[36] T.-H. Loh, Non-invasive measurement of electrically small ultra-wideband and smart antennas, in: Antennas and Propagation Conference, 2013, pp. 456–460.
[37] J.L. Araque, Efficient filtering of cable interaction in small antenna measurements, in: ANTEM, 2010, pp. 1–3.
[38] G. Bao, K. Pahlavan, L. Mi, Hybrid localization of microrobotic endoscopic capsule inside small intestine by data fusion of vision and RF sensors, IEEE Sens. J. 15 (5) (2015) 2669–2678.
[39] V. Prokhorenko, V. Ivashchuk, S. Korsun, S. Musiyachenko, V. Borodavka, Topographic correction of GPR profile based on odometer and inclinometer data, in: International Conference Ground Penetrating Radar, June 2012, pp. 425–429.
[40] M. Wahbah, M. Alhawari, B. Mohammad, H. Saleh, M. Ismail, Characterisation of human body-based thermal and vibration energy harvesting for wearable devices, IEEE Circuits Syst. Mag. 4 (3) (2014) 354–363.
[41] E. Shahhaidar, B. Padasdao, R. Romine, C. Stickley, O. Buric Lubecke, Electromagnetic respiratory effort harvester: human testing and metabolic cost analysis, Biomed. Health Inform. 19 (2) (2015) 399–405.
[42] Q. Zhang, Y. Wang, E. Sok Kim, Electromagnetic energy harvester with flexible coils and magnetic spring for 1–10 Hz resonance, J. Microelectromech. Syst. 24 (4) (2015) 1193–1206.
[43] M. Deterre, E. Lefeuvre, Y. Zhu, M. Woytasik, B. Boutaud, R. Dal Molin, Micro blood pressure energy harvester for intracardiac pacemaker, J. Microelectromech. Syst. 23 (3) (2014) 651–660.
[44] Z. Cheng, Y. Lei, K. Song, C. Zhu, Design and loss analysis of loosely coupled transformer for an underwater high-power inductive power transfer system, IEEE Trans. Magn. 51 (7) (2014) 8401110.